Heat-conserving three-temperature model for ultrafast demagnetization in nickel

M. Pankratova [1,*] I. P. Miranda [1] D. Thonig [1,2] M. Pereiro,[1] E. Sjöqvist,[1] A. Delin,[3,4] O. Eriksson,[1,2] and A. Bergman[1]

[1]*Department of Physics and Astronomy, Uppsala University, Box 516, SE-75120 Uppsala, Sweden*
[2]*School of Science and Technology, Örebro University, SE-701 82 Örebro, Sweden*
[3]*Department of Applied Physics, School of Engineering Sciences, KTH Royal Institute of Technology, AlbaNova University Center, SE-10691 Stockholm, Sweden*
[4]*SeRC (Swedish e-Science Research Center), KTH Royal Institute of Technology, SE-10044 Stockholm, Sweden*

Multireservoir models are widely used for modeling and interpreting ultrafast magnetization dynamics. Here we introduce an alternative formulation to existing three-temperature models for the treatment of spin, electron, and lattice temperatures in magnetization dynamics simulations. In contrast to most existing models of calculations of energy transfer between reservoirs in these types of simulations, the heat distribution of the spin and lattice subsystems is evaluated during the simulation instead of being calculated *a priori*. The model is applied to investigate the demagnetization and remagnetization of fcc Ni, when subjected to a strong laser pulse. In particular, our model results in a fast interplay between the electron and spin subsystems which reproduces the main features of experimental data for fcc Ni significantly better than most reported three-temperature models. We also show that the way in which the electron, spin, and lattice heat capacities are described can have a significant impact on the simulated ultrafast dynamics. By introducing spin-lattice couplings in the simulation, it is shown that these explicit interactions only have a marginal impact on the magnetization dynamics of fcc Ni, albeit it is more pronounced for higher laser pulse powers.

I. INTRODUCTION

Ultrafast control of magnetism is an intense research field, with reports on switching times in the subpicosecond regime. The pioneering work by Beaurepaire *et al.* [1] demonstrated dynamics on a picosecond time scale. The experiment reported in Ref. [1] used a high-intensity laser pulse to pump a nickel sample, and after a time delay a second laser pulse was used to probe its magnetic state, via the magneto-optical effect. To describe ultrafast dynamical processes in such experiments, a so-called two- [2,3] or three-temperature model (3TM) [1,4] has often been used as well as the more recently proposed microscopic 3TM [5] and modified two-temperature model (s-TTM) [3]. The two-temperature model is often applied for a description of nonmagnetic systems, by considering the lattice and the electrons as two coupled heat baths. For magnetic systems, it is important to also take into account the spin reservoir. Therefore, various modifications of the two-temperature model have been proposed; for example, s-TTM assumes a common temperature for the electronic and magnetic systems. In s-TTM, it is assumed that the electron and spin systems are coupled in an energy-conserving way. In

this model, the spin temperature is first calculated using atomistic spin dynamics simulations and then subtracted from the electron one. Direct spin-lattice coupling (SLC) is not taken into account. This modified two-temperature model seems to capture the main features of energy transfer between the spin and lattice subsystems. Another model often applied for the description of ultrafast processes of magnetic materials is a three-temperature model, where atomic spin moments, ions, and electrons each have their own temperature/heat reservoir and heat is allowed to flow between reservoirs via coupled differential equations. This model is used either to analyze a particular experimental result, e.g., as done in Ref. [1], or as a key ingredient in atomistic simulations of magnetization dynamics [6,7].

In addition to the aforementioned two-temperature model and 3TM, many other models have been proposed to explain the underlying mechanisms governing ultrafast demagnetization [8] and how angular momentum is transferred between subsystems. For example, the role of spin-dependent transport of laser-excited electrons was discussed in Ref. [9], whereas in Ref. [10] the focus was put on the optical intersite spin transfer as the main mechanism responsible for the ultrafast demagnetization. The impact of Elliott-Yafet electron-phonon spin-flip scattering was investigated in Ref. [11].

Among the shortcomings of 3TM is, first of all, the fact that it includes several coupling parameters that are unknown or at least difficult to estimate. This relates in particular to the parameters describing the electron-lattice, electron-spin, and spin-lattice coupling. From literature in the field (see [1,3,12,13] and references therein) it may be noted that the values of these coupling parameters can vary with more

*maryna.pankratova@physics.uu.se

than one order of magnitude (see Appendix C), which makes an accurate description of the experimental observations very challenging. Reference [13] corroborates this argumentation and there it has been shown that the value of the electron-phonon heat transfer parameter extracted from experimental data using the two-temperature model and that from *ab initio* calculations disagree significantly. This clearly calls for a model that reduces the number of uncertain coupling parameters. Another disadvantage of the 3TM model is that both spin and lattice heat capacities are often assumed to be independent of temperature, which clearly is an approximation. The importance of temperature-dependent spin capacities especially for temperatures close to the Curie point was discussed in Ref. [5] in refined microscopic 3TM [5,14]. Combined temperature-dependent spin and electron capacities were also introduced for s-TTM in Ref. [3].

The somewhat uncontrolled aspects of the 3TM have lead to conclusions that atomistic spin dynamics simulations fail to successfully describe the initial demagnetizing phase (i.e., the first 500 fs) during ultrafast demagnetization processes (see, e.g., Ref. [15]). This statement is partially based on physical insights that the precession frequency of atomic spins in a ferromagnet is too low to describe the short (subpicosecond) time scales of pump-probe experiments like the ones presented in Ref. [1]. This conclusion is also based on a direct comparison between experiments and simulations that rely on the 3TM model, e.g., as was done for Co_2FeAl [15]. Our goal is here to identify an improved description of how heat is transferred between the electron, spin, and lattice reservoirs in the demagnetization processes of ultrafast pump-probe experiments, and to investigate if it can improve the agreement between observation and simulation, in particular, the spin dynamics in the subpicosecond time scale. Of relevance for this paper, it should be noted that the model based on atomistic spin dynamics as proposed by Zahn *et al.* [3,8] also uses energy-conserving atomistic spin dynamics simulations, and the authors of Refs. [3,8] considered ultrafast demagnetization of nickel [3], iron, and cobalt [8]. However, the model of Zahn *et al.* includes an electron-lattice heat transfer coefficient and the impact of spin-lattice interaction was not considered.

The structure of the paper is as follows. First, we briefly present the details of spin-lattice atomistic spin dynamics simulations. Then, In Sec. III a heat-conserving three-temperature model (HC3TM) is introduced. In Sec. IV we demonstrate how the heat-conserving three-temperature model, in combination with atomistic spin dynamics simulations, reproduces the observed, ultrafast magnetization dynamics of fcc Ni. We also investigate the influence of spin-lattice coupling on the magnetization dynamics.

II. SPIN-LATTICE DYNAMICS SIMULATIONS

The time evolution of spin and lattice is obtained using Langevin dynamics simulations, as described in Ref. [16]:

$$\frac{d\boldsymbol{m}_i}{dt} = -\frac{\gamma}{(1+\alpha^2)}\boldsymbol{m}_i \times \left(\boldsymbol{B}_i + \boldsymbol{B}_i^{fl}\right) - \frac{\gamma}{(1+\alpha^2)}\frac{\alpha}{m_i}\boldsymbol{m}_i$$
$$\times \left(\boldsymbol{m}_i \times \left[\boldsymbol{B}_i + \boldsymbol{B}_i^{fl}\right]\right), \quad (1)$$

$$\frac{d\boldsymbol{u}_k}{dt} = \boldsymbol{v}_k, \quad (2)$$

$$\frac{d\boldsymbol{v}_k}{dt} = \frac{\boldsymbol{F}_k}{M_k} + \frac{\boldsymbol{F}_k^{fl}}{M_k} - \nu\boldsymbol{v}_k \quad (3)$$

where m_i is an atomic magnetic moment. Effective magnetic field $\boldsymbol{B}_i = -\partial H_{SLD}/\partial \boldsymbol{m}_i$ is obtained from spin-lattice Hamiltonian H_{SLD}, which in our case includes magnetic, lattice, and spin-lattice coupling parts similar to Ref. [16]. All parameters necessary for spin-lattice dynamics simulations, such as exchange interactions, magnetic moments, forces, and spin-lattice couplings, were obtained from *ab initio* calculations (see Appendix B for details). Effective force at site k is determined by $\boldsymbol{F}_k = -\partial H_{SLD}/\partial \boldsymbol{u}_k$. M_k is the mass of the atom at site k, m is the saturation magnetization, γ is the gyromagnetic ratio, while α and ν are Gilbert and lattice damping constants, respectively. We model stochastic fields $\boldsymbol{B}_i^{fl}$ and $\boldsymbol{F}_k^{fl}$ as white noise with properties $\langle B_{i,\mu}^{fl}(t)B_{j,\nu}^{fl}(t')\rangle = 2D_M\delta_{ij}\delta_{\mu\nu}(t-t')$ and $\langle F_{i,\mu}^{fl}(t)B_{j,\nu}^{fl}(t')\rangle = 2D_L\delta_{kl}\delta_{\mu\nu}(t-t')$. In our calculations, we use $D_M = \alpha k_B T/\gamma m$ and $D_L = \nu M k_B T$, where T and k_B are temperature and Boltzmann constant correspondingly.

III. HEAT-CONSERVING THREE-TEMPERATURE MODEL

The model proposed here describes the temperature induced fluctuations and dissipation from Langevin dynamics given by Eqs. (1)–(3), where both the spin and lattice systems have effective damping terms α (for spin) and ν (for lattice), unique for each reservoir, and where both systems are coupled to the electronic system. Both systems are coupled to the electronic heat bath, such that it is the electronic temperature that governs the magnitude of the fluctuations that enter the equations of motion of the spin and lattice systems. The resulting spin and lattice temperatures are then determined from measurements during the spin-lattice simulations. If the electronic temperature is driven to be higher than the lattice and spin temperatures, fluctuations from this elevated electronic temperature will cause an increase of the lattice and spin temperature, signaled by transiently increased fluctuations of these subsystems. For heat conservation to take place, the electronic temperature then has to decrease and this is modeled by considering that the same amount of heat that flows into the spin and lattice reservoirs needs to be removed from the electronic system. This can be expressed as a time dependent temperature profile obeying the relation

$$\Delta T_e(t) = -\frac{C_l(T_l)}{C_e(T_e)}T_l(t) - \frac{C_s(T_s)}{C_e(T_e)}T_s(t) + \frac{W(t)}{C_e(T_e)}, \quad (4)$$

where T_l is calculated from the average kinetic energy of the lattice vibrations, $\langle E_l^{kin}\rangle/k_B$. Similarly, T_s is obtained as an average of the exchange energy of the ensemble of atomic spins, i.e., $\langle E_s^{xc}\rangle/k_B$ [17]. The definition of an instantaneous measure of the temperatures in an out-of-equilibrium system is not obvious [18], but is still typically assumed to hold in these kinds of models. Introducing a time average of the temperatures, for narrow time windows, does not, however, change our results significantly. In addition, Eq. (4) contains the temperature-dependent specific heats of the electron, lattice,

and spin systems, C_e, C_l, and C_s, respectively. The possibility for an external stimuli, e.g., a laser, to momentarily increase the temperature of the electronic subsystem is captured by the source term $W(t)$ which is modeled as a Gaussian.

Hence, instead of 3TM equations proposed in Ref. [1] we introduce the following procedure to calculate spin, electron, and lattice temperatures.

(i) From Eqs. (1)–(3) at every time step we calculate lattice and spin temperatures using the expressions $T_l = \langle E_l^{\mathrm{kin}}\rangle/k_B$ and $T_s = \langle E_s^{xc}\rangle/k_B$.

(ii) The change of electronic temperature from the initial one (in our case 300 K) is then calculated using Eq. (4) for every time step t.

Some recent works, for example, Ref. [13], point out that a single lattice temperature is not sufficient to describe experimental data. However, the difference between simulations and experiment observed in Ref. [13] may partly be connected to the uncertain estimation of G_{el} (see Appendix C). The difference between data extracted from experiments, using the two-temperature model, and calculated values is seen to be significant. Furthermore, it is shown in Refs. [3,8] that using atomistic spin dynamics simulations one can successfully describe magnetization dynamics of iron, cobalt, and nickel with only single lattice temperature.

In practical calculations of Eq. (4) the common approximation is made that the electronic heat capacity is proportional to the electronic temperature; $C_e = \gamma_e T_e$, and for fcc Ni we use $\gamma_e = 6 \times 10^3\,\mathrm{J\,m^{-3}\,K^{-2}}$ [1]. Furthermore, realistic heat capacities for the lattice were obtained analytically from the Debye model [19] (with $\theta_D = 475$ K [20]), while for the spin reservoir heat capacity is calculated using Monte Carlo and atomistic spin dynamics simulations incorporating quantum (Bose-Einstein) statistics and following the procedure described in detail in Ref. [21] (see Appendix A2 for details). Usage of Bose-Einstein statistics is beneficial in comparison with calculations from classical statistics because it allows a more accurate description of capacities at low temperatures, although it can overestimate capacities around T_C.

IV. RESULTS

A. Ultrafast demagnetization of fcc Ni

In order to distinguish between different models of heat transfer between subsystems, the conventional three-temperature model is below referred to as 3TM (please see Appendix A 1 and Ref. [1] for model details), while the here suggested model [Eq. (2)] is referred to as the HC3TM. We focus here on ultrafast demagnetization of fcc Ni, and to compare outcomes of the conventional 3TM with the HC3TM model we employ spin-lattice dynamics simulations in the temperature range of $T \in [300, 550]$ K, for simulation cells with a $60 \times 60 \times 60$ repetition of the fcc unit cell, using periodic boundary conditions. In addition, $N_t = 1 \times 10^6$ time steps of $dt = 10^{-16}$ s were used in combination with other parameters presented in Table I. First, we present temperature profiles (Fig. 1) for spin, lattice, and electron subsystems for a laser fluence of $5\,\mathrm{J/m^2}$. These results were obtained from conventional 3TM as well as HC3TM, using either fixed or variable heat capacities. Other parameters relevant

TABLE I. List of the parameters used in the simulations.

Parameter	Value
γ_e	$6 \times 10^3\,\mathrm{J\,m^{-3}\,K^{-2}}$
HC3TM parameters	
Gilbert damping α	0.024[a]
Lattice damping ν	$\approx 1.0\,\mathrm{ps^{-1}}$ [b]
3TM parameters	
G_{el}	$8 \times 10^{17}\,\mathrm{W\,m^{-3}\,K^{-1}}$
G_{es}	$6 \times 10^{17}\,\mathrm{W\,m^{-3}\,K^{-1}}$
G_{sl}	$0.3 \times 10^{17}\,\mathrm{W\,m^{-3}\,K^{-1}}$

[a]The Gilbert damping value was obtained considering the experimental relaxation rate $\lambda = \alpha\gamma m$, in SI units, of 2.9×10^9 s^{-1} for fcc Ni in the easy axis ([111]) [22,23], which was converted to the dimensionless α parameter following Fig. 1 in Ref. [22].
[b]This is equivalent to the lattice damping parameter $\gamma_{el} = 1 \times 10^{-13}$ kg/s in the notation of Ref. [24].

for these simulations are listed in Table I. It can be seen from Fig. 1 that, compared to 3TM, HC3TM results in faster thermalization between the three reservoirs, in particular when variable heat capacities are considered. In addition, the overall time dependence of the temperature profiles from HC3TM, especially with variable heat capacities, is faster than the conventional 3TM. When comparing 3TM and HC3TM one needs to take into account the relation between the model parameters. In particular, the relation between the G_{el} of 3TM and lattice damping was obtained in Ref. [24], which for $G_{el} = 8 \times 10^{17}\,\mathrm{W\,m^{-3}\,K^{-1}}$ gives the value of the lattice damping $\nu \approx 0.2$ ps^{-1}. We demonstrated above the results for the lattice damping value $\nu \approx 1.0$ ps^{-1} because temperature profiles in this case are closer to the experimentally obtained ones. However, a temperature profile for the damping 0.2 ps^{-1} can be found in Appendix A1.

In Fig. 2 the magnetization dynamics are shown for 3TM and HC3TM with either constant or varying heat capacity. It can be seen from the figure that HC3TM results in faster
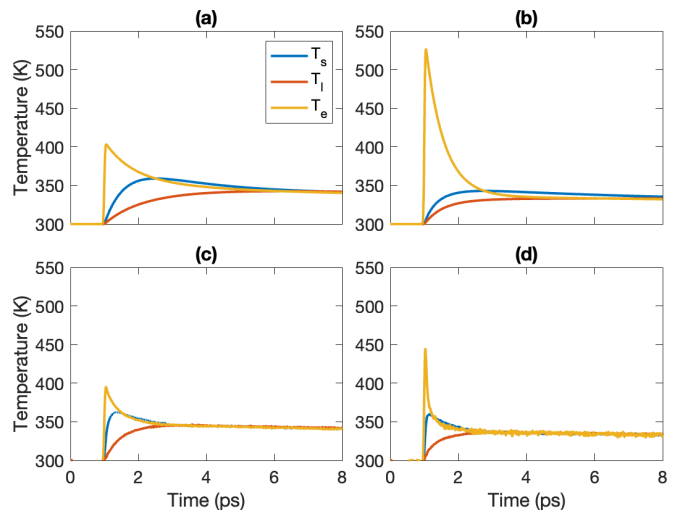

FIG. 1. Spin T_s (blue line), lattice T_l (red line), and electron temperatures T_e (yellow line) calculated from 3TM (a, b) or HC3TM (c, d) with constant (a, c) or variable (b, d) capacities.
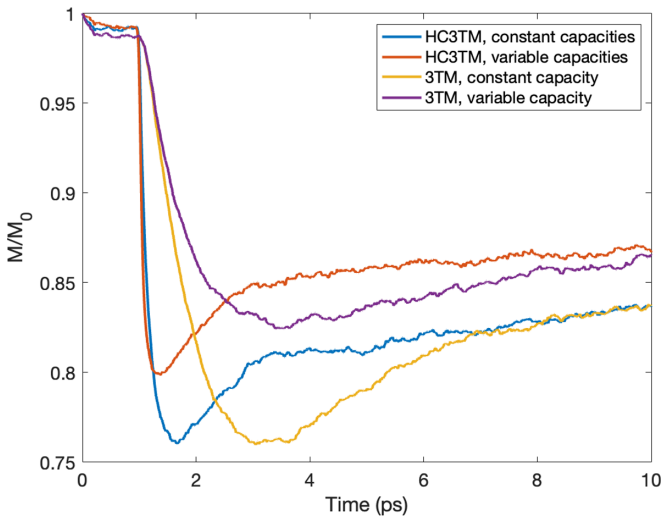
FIG. 2. Normalized magnetization of fcc Ni vs time in 3TM and HC3TM with constant or variable capacities, for a laser pulse with fluence of 5 J/m^2.

magnetization dynamics during the first picoseconds and faster recovery of the magnetization, when compared to 3TM. It can also be seen that the choice of constant or variable heat capacities does not affect the demagnetization speed in the first ≈ 300 fs, for either model of the heat transfer. The figure also shows that HC3TM and 3TM reaches roughly the same value of magnetic moment, in the maximally demagnetized state, albeit at noticeably different times. The faster demagnetization for the HC3TM case occurs since the heat bath for the spins is here governed by the electron temperature which rises faster than the *a priori* determined spin temperature in the 3TM. As a final remark to the results in Fig. 2, we note that for both models a constant heat capacity results in a more pronounced demagnetized state (lower value of the magnetization), something which is most conspicuous for the 3TM. The experimental curves published in Ref. [1] have a minimum value of the magnetization at around 1 ps, and a demagnetized state of $M/M_0 \approx 0.53$. This can be compared to the results in Fig. 2, and we note that overall the here suggested HC3TM captures experimental data with better precision than the conventional 3TM. For instance, as Fig. 2 shows, the minimum of the M/M_0 curve is for the HC3TM model with calculated specific heats placed close to 1 ps, in agreement with observations. The direct comparison of simulation results with experimental data is, however, a challenging task. Concretely, in Ref. [24] the authors note that to match experimental data they adjusted both damping value and pulse fluence. They explain this by the fact that the fraction of the pulse energy that is transferred to the electrons in experiments is not clear. Another successful attempt to fit simulations with experimental data was made in Ref. [25]; however, to reach the agreement the fitting parameter was used with its physical origin not clear. In Ref. [3] good agreement with experimental data was obtained for a given value of laser pulse fluence. Damping and G_{el} were obtained from density functional theory (DFT) calculations but G_{es} was considered infinitely large. Moreover, the obtained value of G_{el} significantly differs from that used in Ref. [1] and some

calculated values, but coincides with some other works (see Ref. [3] and references therein). This again returns to the point of difficulty of estimation of G_{el} and, therefore, the need in reducing the number of coupling constants in the model. To some extent this is also true for the model introduced in this paper where change to either the Gilbert spin damping, the lattice damping, or the fluence absorption ratio changes the behavior of the demagnetization process. Comparing the 3TM and HC3TM models, as is the focus of this paper, for the same set of equivalent coupling parameters and laser fluence, we do however always find a distinctively faster demagnetization for the HC3TM model compared to the 3TM simulations. The main explanation for the faster demagnetization dynamics in the case of HC3TM can be traced back to the fact that in HC3TM it is the electron heat bath that enters the Langevin term that governs the fluctuations and dissipations of the spin dynamics in the simulations. The crucial influence of the electron heat bath indicates that the direct lattice contribution on the spin system is limited, and that is examined in more detail in the next section.

B. Impact of spin-lattice coupling

In Ref. [16] it was shown that spin-lattice coupling can be treated in coupled spin-lattice simulations, by a dependence of the exchange interaction, J_{ij}, on atomic displacements u_k. The spin-lattice term in the Hamiltonian can be obtained by Taylor expanding the magnetic bilinear Hamiltonian with respect to the lattice displacements. This results in a spin-lattice coupling term that is in general bilinear in spin and linear in displacements [16]. The components of the spin-lattice coupling terms were here calculated for fcc Ni, by taking into account various number of neighbors in the Taylor expansion. To be specific, we obtained coupling tensor values when taking into account first, second, third, and fourth neighbors of the lattice displacement. Calculated values of these parameters were used to study the impact of spin-lattice coupling on fcc Ni, using the same type of simulations as presented in Figs. 1 and 2. The introduction of these explicit spin-lattice couplings allows for a direct exchange of heat between the spin and lattice subsystems. Compared to existing temperature models these atomistic spin-lattice couplings would be analogous to a microscopic magnon-phonon coupling which enters into the regular 3TM.

We have investigated the impact of spin-lattice coupling in both 3TM and HC3TM, by performing coupled spin and lattice dynamics simulations [16], a model we refer to here to as SLD. Our results show that for fcc Ni the introduction of explicit spin-lattice coupling terms in SLD simulations only has a marginal impact on the demagnetization (Fig. 3) compared to when the spin and lattice dynamics are simulated without the spin-lattice coupling. In Fig. 3 we compare results from spin dynamics simulations and coupled SLD simulations, using the HC3TM model with variable capacities for heat transfer between reservoirs. It can be seen from the figure that spin-lattice coupling treated in SLD simulations only has a minimal impact on the demagnetization speed of fcc Ni. Primarily, this can be explained by the fact that the spin-lattice coupling in fcc Ni is weak. The limited spin-lattice coupling effect on our simulations could also partially be caused by
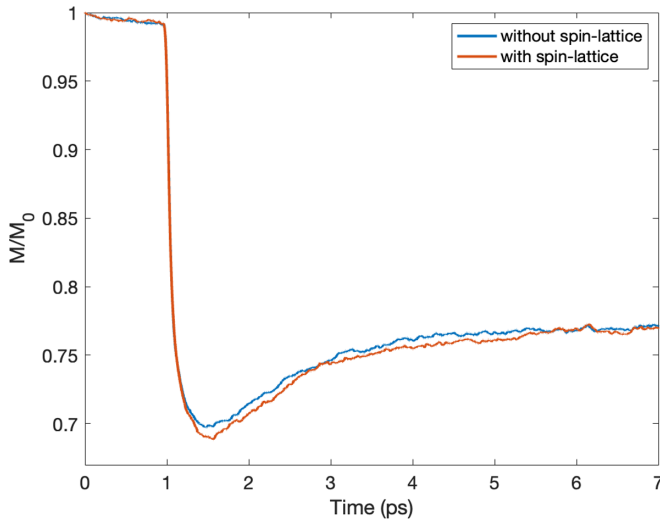
FIG. 3. Impact of spin-lattice coupling on magnetization dynamics in HC3TM with variable capacities following the application of laser pulse with fluence 8 J/m^2.

limitations on the model for the SLD simulations where the spin-lattice term cannot fully describe the transfer of angular momentum between the spin and lattice subsystems [16].

V. CONCLUSIONS

We propose a HC3TM to calculate spin, electron, and lattice temperature in ultrafast demagnetization simulations. One benefit of the HC3TM model is that it reduces the number of heat transfer parameters, the values of which are difficult to define experimentally. The main strength of the model is, however, that it produces a qualitatively correct time scale for the demagnetization process, something that most earlier 3TM models have failed to do. The main reason for why the HC3TM captures the demagnetization so well, despite previous arguments that atomistic spin dynamics simulations are inadequate in describing subpicosecond processes, is the direct coupling between the electron heat bath and the fluctuations in the spin subsystem. This is in line with the recent findings of Zahn *et al.* [3], where an infinite coupling between electrons and spins was assumed.

We have demonstrated by simulating magnetization dynamics of fcc Ni after the application of a femtosecond laser pulse of 5 J/m^2 that the HC3TM model reproduces experimental observations with higher accuracy, compared to the 3TM. We also investigated the impact of temperature-dependent spin and lattice capacities on magnetization dynamics, both in the 3TM and the HC3TM. We find that for both models a dynamic evaluation of the specific heats is important. Finally, the impact of spin-lattice coupling on magnetization dynamics was investigated and it was shown that for fcc Ni the spin-lattice coupling has almost no impact.

The here suggested HC3TM is expected to be relevant in general as a tool for simulations of magnetization dynamics in the ultrafast regime. There are currently significant efforts in pump-probe experiments [5,26–29], of the nature pioneered by Ref. [1]. These experimental investigations have been followed by equally intense theoretical works [3,12,24,29–32].

In methods based on an atomic description of the dynamics, there is a difficulty in establishing mechanisms for heat transfers between electron, spin, and lattice reservoirs, and we believe the method proposed here is a significant step forward. In this paper we chose to exemplify our method by applying it to fcc Ni. This choice was primarily motivated by the fact that the original experimental work of Ref. [1] was for fcc Ni. In a sense this choice was less optimal, since the treatment here is based on a classical spin description, and fcc Ni is known to be less well described as a classical system. Despite this, agreement between experiments and theory, e.g., as shown in Fig. 2, is rather good, and we expect that this agreement would be even better for systems that are naturally described with an atomic description of the magnetism. Such studies are underway, and we note that most of the materials investigated in the field, both from experiments and from theory, are of this nature.

APPENDIX A: DETAILS OF 3TM AND HC3TM CALCULATIONS

1. Three-temperature model

The three-temperature model was proposed by Beaurepaire *et al.* in 1996 [1], and it describes transfer of heat between the spin, electron, and lattice reservoirs. The evolution of the system is then described by the coupled differential equations:

$$C_e(T_e)\frac{dT_e}{dt} = -G_{el}(T_e - T_l) - G_{es}(T_e - T_s) + P(t),$$

$$C_s(T_s)\frac{dT_s}{dt} = -G_{es}(T_s - T_e) - G_{sl}(T_s - T_l),$$

$$C_l(T_l)\frac{dT_l}{dt} = -G_{el}(T_l - T_e) - G_{sl}(T_l - T_s). \quad (A1)$$

In these equations, T_e, T_s, and T_l represent the temperatures of electron, spin, and lattice reservoirs, respectively, while C_e, C_s, and C_l are the corresponding specific heats. Coupling between the different reservoirs is provided by G_{es}, G_{el}, and G_{sl}, while $P(t)$ represents the effect provided by the laser in the pump process.

2. Heat capacity of the spin subsystem

In our calculations for 3TM and HC3TM, we use temperature-dependent heat capacity of the spin subsystem.
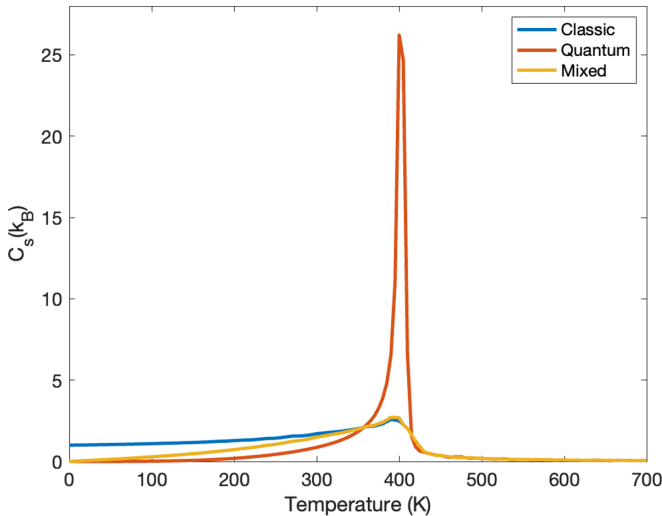
FIG. 4. Temperature-dependent spin capacities obtained for fcc Ni obtained using different statistical approaches.

FIG. 5. Spin, lattice, and electron temperatures obtained in HC3TM with variable heat capacities, for a lattice damping value $\nu \approx 0.2 \, \mathrm{ps}^{-1}$ (or 2×10^{-14} kg/s). The other parameters are the same as in a previous case.

However, there exist several approaches to calculating it. In particular, the widely applied classical approach which uses Boltzmann statistics is known to overestimate heat capacity at low temperatures leading to the limit 1 k_B at $T \to 0$ (see the red curve in Fig. 4) and this disagrees with experimental data. On the other hand more recently proposed [21] calculations from quantum statistics can address the issue at low temperatures but overestimate the capacity around T_c as can be seen from Fig. 4. Finally, one can combine the benefits of these two methods by using the quantum approach at low temperatures and then switching back to the classical one. This results in the heat capacity of the spin system presented by the blue curve in Fig. 4. A more detailed description of these methods can be found in Ref. [33].

In our simulations, we used variable capacity obtained from quantum statistics. In the presented results the spin temperature never reaches the T_c and therefore our results are not affected by overestimating C_s close to T_c. Moreover, our tests show that the main results of HC3TM are preserved and the only thing that is impacted by the change of capacities is a drop in the magnetization. The difference between the mixed and quantum approaches is only marginal; however, the difference in magnetization drop with the classical case is more significant. The main outcome of the HC3TM—high demagnetization speed and the position of the magnetization minimum—remains the same for all three capacities. Finally, 3TM is more sensitive to the change of variable capacities. When using classical heat capacity demagnetization is much slower than obtained by HC3TM or observed in Ref. [1]. However, one can obtain a close to experimental demagnetization rate by using variable spin capacity from quantum statistics in 3TM.

3. Benchmark of 3TM and HC3TM

In Fig. 1 the lattice damping value was chosen to ensure close agreement with experimental data. However, for more precise comparison between 3TM and HC3TM one can use the relation between the G_{el} of 3TM and lattice damping
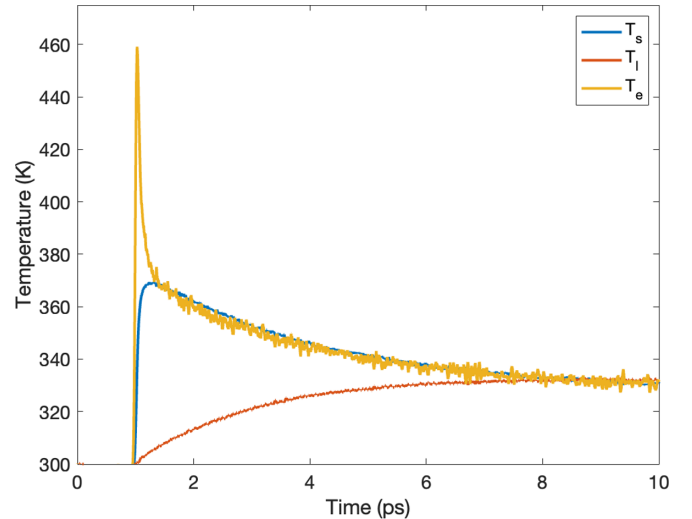
from Ref. [24], which for $G_{el} = 8 \times 10^{17} \, \mathrm{W \, m^{-3} \, K^{-1}}$ gives the value of the lattice damping $\nu \approx 0.2 \, \mathrm{ps}^{-1}$ (or 2×10^{-14} kg/s). In Fig. 5 spin, lattice, and electron temperatures are presented for the lattice damping values corresponding to G_{el} given in Table I.

We stress that the change of lattice damping does not impact the main features of the heat-conserving 3TM, for example, higher demagnetization speed. The decrease of lattice damping leads mostly to longer thermalization of the system.

APPENDIX B: DETAILS OF THE ELECTRONIC STRUCTURE CALCULATIONS

In order to make the theory material specific, we calculate all parameters necessary for the coupled spin and lattice dynamics simulations from electronic structure theory. This has been done by means of DFT with the fully self-consistent real-space linear muffin-tin orbital method in the atomic sphere approximation (RS-LMTO-ASA) [34,35]. The Ni bulk was treated in real space, involving in the continued fraction steps a large cluster of 47 500 atoms in the fcc crystal positions, with the experimental lattice parameter of $a = 3.52 \, \mathrm{\AA}$ [36]. Here, we work in the orthogonal representation of the LMTO-ASA [37] and expand the Hamiltonian within a tight-binding basis, where terms of the second order in energy (or higher)

TABLE II. Lattice parameter, spin (m_{spin}), and orbital (m_{orbital}) of fcc Ni.

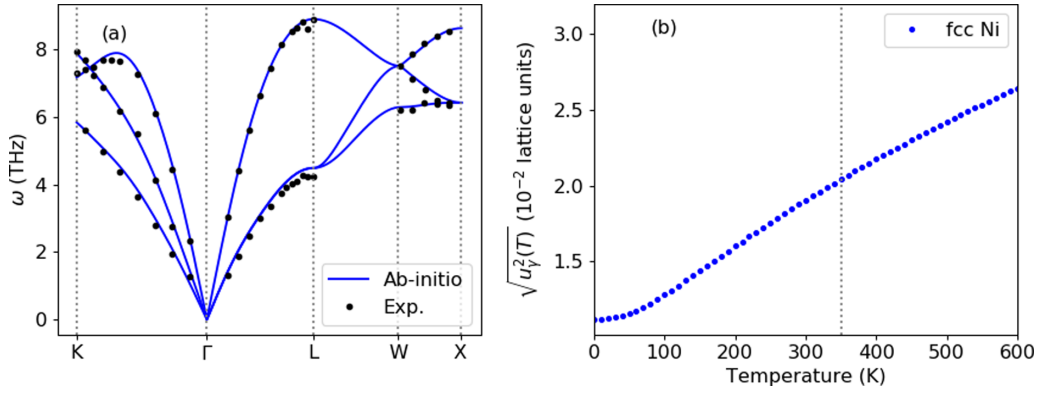|	a (Å)	m_{spin} (μ_B)	m_{orbital} (μ_B)
RS-LMTO-ASA (LSDA)	3.52	0.71	0.04
QE/USPP (GGA)	3.52	0.67	
Expt. [36]	3.524	0.57	0.05

FIG. 6. (a) Computed phonon dispersion for bulk fcc Ni (blue solid lines) compared to inelastic neutron scattering data (black dots) from Ref. [51]. (b) Calculated root-mean-square thermal displacements of Ni atoms for each Cartesian direction, $\sqrt{u_\gamma^2(T)}$, as a function of temperature, in units of a. The vertical dotted line at 350 K is just a mark for the upper bound of the lattice temperature (T_l, see main text) achieved during the three-temperature model simulations.

are neglected [38,39]. The calculations were carried out considering the local spin-density approximation (LSDA) with the exchange and correlation potential of von Barth and Hedin [40]. The spin-orbit (ls) coupling is included at each variational step [37,41]. In the recursion method, the Beer-

TABLE III. Absolute values of elements $\phi_{0j}^{\alpha\beta}$ of the force constant matrices of fcc Ni, in units of mRy/Å², obtained for a $6 \times 6 \times 6$ supercell and using the same type of notation as in Ref. [52]. Here, j stands for the neighborhood shell around the reference site. The atomic positions are given in units of lattice constant, a.

j	Atom position	Force constant matrix	Ab initio values
1	$\frac{1}{2}(1, 1, 0)$	$\begin{pmatrix} \alpha_1 & \beta_1 & 0 \\ \beta_1 & \alpha_1 & 0 \\ 0 & 0 & \gamma_1 \end{pmatrix}$	$\alpha_1 = 77.85$ $\beta_1 = 86.24$ $\gamma_1 = 0.07$
2	$\frac{1}{2}(2, 0, 0)$	$\begin{pmatrix} \alpha_2 & 0 & 0 \\ 0 & \beta_2 & 0 \\ 0 & 0 & \beta_2 \end{pmatrix}$	$\alpha_2 = 8.85$ $\beta_2 = 3.62$
3	$\frac{1}{2}(2, 1, 1)$	$\begin{pmatrix} \alpha_3 & \gamma_3 & \gamma_3 \\ \gamma_3 & \beta_3 & \delta_3 \\ \gamma_3 & \delta_3 & \beta_3 \end{pmatrix}$	$\alpha_3 = 5.50$ $\beta_3 = 2.25$ $\gamma_3 = 3.12$ $\delta_3 = 0.28$
4	$\frac{1}{2}(2, 2, 0)$	$\begin{pmatrix} \alpha_4 & \beta_4 & 0 \\ \beta_4 & \alpha_4 & 0 \\ 0 & 0 & \gamma_4 \end{pmatrix}$	$\alpha_4 = 1.15$ $\beta_4 = 0.73$ $\gamma_4 = 0.23$
5	$\frac{1}{2}(3, 1, 0)$	$\begin{pmatrix} \alpha_5 & \delta_5 & 0 \\ \delta_5 & \beta_5 & 0 \\ 0 & 0 & \gamma_5 \end{pmatrix}$	$\alpha_5 = 0.32$ $\beta_5 = 0.41$ $\gamma_5 = 0.55$ $\delta_5 = 0.28$
6	$\frac{1}{2}(2, 2, 2)$	$\begin{pmatrix} \alpha_6 & \beta_6 & \beta_6 \\ \beta_6 & \alpha_6 & \beta_6 \\ \beta_6 & \beta_6 & \alpha_6 \end{pmatrix}$	$\alpha_6 = 0.23$ $\beta_6 = 0.41$
7	$\frac{1}{2}(3, 2, 1)$	$\begin{pmatrix} \alpha_7 & \delta_7 & \epsilon_7 \\ \delta_7 & \beta_7 & \eta_7 \\ \epsilon_7 & \eta_7 & \gamma_7 \end{pmatrix}$	$\alpha_7 = 0.78$ $\beta_7 = 0.09$ $\gamma_7 = 0.14$ $\delta_7 = 0.28$ $\epsilon_7 = 0.55$ $\eta_7 = 0.46$

Pettifor [42] terminator is used, and the recursion chain is terminated after 31 levels.

The Heisenberg exchange interactions were calculated using the Liechtenstein-Katsnelson-Antropov-Gubanov scheme [43] as implemented in the RS-LMTO-ASA code [39]. We also calculated the spin-lattice parameters, as described in Ref. [16], i.e., $\Gamma_{ijk}^{\alpha\beta\gamma} = \frac{\partial \mathcal{J}_{ij}^{\alpha\beta}}{\partial u_k^\gamma}\big|_{u_k^\gamma=0}$ (α, β, γ are Cartesian indices). These parameters were computed directly, by considering the changes in the calculated $\mathcal{J}_{ij}^{\alpha\beta}$ tensors when displacements of atomic positions, $|u_k^\gamma| \leqslant 0.02a$ in the $\gamma = \{\pm x, \pm y, \pm z\}$ directions, were considered. To represent the final $\mathcal{J}_{ij}^{\alpha\beta}(u_k^\gamma)$ function, we fitted a first-order polynomial, from which the calculation of the $\Gamma_{ijk}^{\alpha\beta\gamma}$ parameters is possible. In our simulations, we considered up to third neighbor spin-lattice parameters (42 interactions), which will be explicitly shown in Appendix B1. Here, we note that direct calculations of the *ab initio* spin-lattice parameters are also feasible (see, e.g., Ref. [44]).

The interatomic forces, needed for the lattice dynamics, were calculated using a combination of QUANTUM ESPRESSO
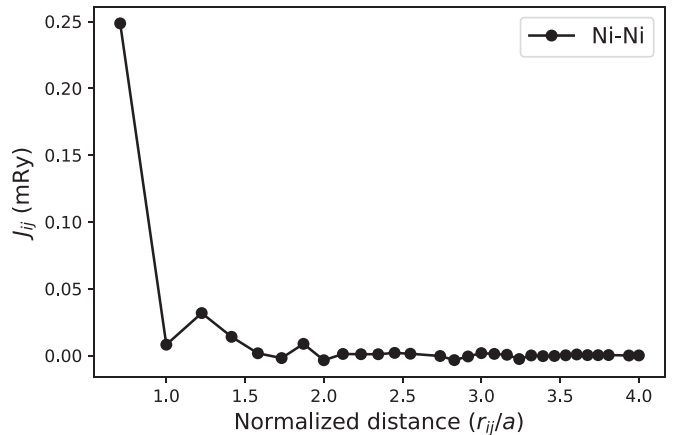

FIG. 7. Computed (i, j) isotropic exchange interactions in fcc Ni as a function of the pairwise distance (in units of the lattice parameter a). Lines are guides for the eyes.
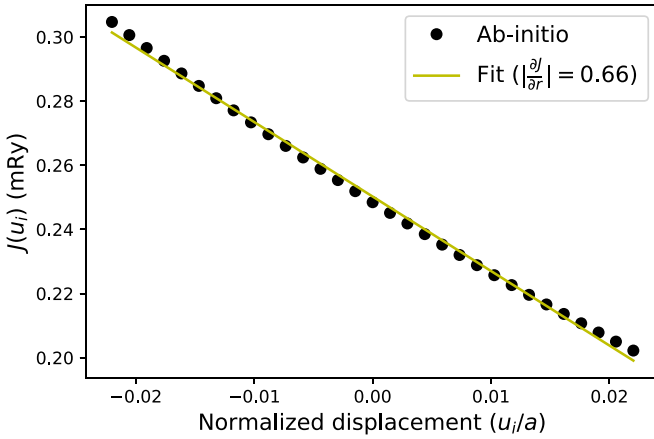
FIG. 8. Computed nearest-neighbor (i, j) Ni-Ni pairwise isotropic exchange interactions as a function of the displacement u_i (in units of the lattice parameter a). The yellow solid line represents a polynomial fit of first order, for which the value of $\frac{\partial J_{ij}}{\partial u_i}|_{u_i=0}$ is given (in units of mRy/Å). Negative displacements ($u_i < 0$) represent a reduction of the pairwise distance, in real space.

(QE) [45] and PHONOPY [46] packages. In QE, we used a scalar-relativistic scheme based on ultrasoft pseudopotentials (USPP) [47] and the Perdew-Burke-Ernzerhof exchange correlation, for which a standard pseudopotential from the QE library was used ($3s$, $3p$, $4s$, and $3d$ valence electrons). A cutoff of 60 (480) Ry was used for the kinetic (charge density) energy. A Monkhorst-Pack (MP) [48] grid of $18 \times 18 \times 18$ $\vec{k}$ points was set for the first Brillouin zone (BZ). Self-consistent calculations with 10^{-10}-Ry convergence threshold were carried out using the Marzari-Vanderbilt [49] smearing with a spreading of 0.01 Ry for BZ integration. The force constants and phonon frequencies were computed based on a $6 \times 6 \times 6$ supercell (216 atoms), where we considered a $3 \times 3 \times 3$ $\vec{k}$-points MP mesh.

1. Calculated properties and interactions of fcc Ni

To validate the electronic structure-based parameters that we have used in the simulations, here we provide a comparison between the computed properties and interactions of fcc Ni with experimental results whenever available. The obtained magnetic moments from both RS-LMTO-ASA and QE

calculations are shown in Table II, with a good agreement with the experimental measurements [36,50].

From QE, we first optimized the fcc Ni structure in order to achieve null forces and internal pressure. The resulting change in the lattice parameter was negligible, i.e., less than $\approx 0.02\%$ of the experimental one. With this structure, the computed phonon frequencies with the $6 \times 6 \times 6$ supercell in PHONOPY are shown in Fig. 6(a) together with inelastic neutron scattering data [51], with which an excellent agreement can be seen. From these phonon dispersion calculations, the force constants $\phi_{ij}^{\alpha\beta}$ (see Ref. [16]), important for the lattice dynamics, were also obtained. The resulting irreducible values and their respective signs, related to the crystal symmetry, are shown in Table III considering up to the seventh neighboring shell of a reference atom at the site $i = 0$ (134 neighbors). The force matrices use the same type of notation as in Ref. [52]. They show a good agreement with other *ab initio* calculations [53], as well as with fits to the experimental phonon frequencies [54]. In order to estimate the range of atomic displacements in fcc Ni as a function of temperature, necessary for the calculation of spin-lattice coupling parameters, we calculated the root-mean-square thermal displacements for each Cartesian direction, $\sqrt{u_\gamma^2(T)}$, as implemented in PHONOPY. As the thermal expansion of Ni can be satisfactorily simulated within the harmonic approximation in the low-temperature regime [55,56], we did not consider here anharmonic effects on $\sqrt{u_\gamma^2(T)}$. The obtained values are shown in Fig. 6(b). Near the greatest obtained lattice temperature ($T_l \lesssim 350$ K, see main text), the calculated displacements are $\approx \pm 0.02a$. This limit is, then, used to guide the maximum displacements of Ni atoms in the RS-LMTO-ASA method, in the $\gamma = \{\pm x, \pm y, \pm z\}$ Cartesian directions, which are equivalent to each other due to the cubic symmetry of fcc Ni. We note that this calculated displacement limit is compatible with both the actual average displacement of individual atoms in the spin-lattice dynamics ($u_\gamma \approx 0.015a$), and the experimental value ($\approx 0.03a$, at 300 K [57]) obtained by fitting to the Debye model.

Figure 7 shows the obtained isotropic exchange interactions, which result in a random-phase approximation Curie temperature of $T_C = 403$ K. For the correspondent isotropic SLCs, $\Gamma_{ijk}^{\alpha\alpha\gamma} = \frac{\partial \mathcal{J}_{ij}^{\alpha\alpha}}{\partial u_k^\gamma}|_{u_k^\gamma=0}$, we find that, when $k \neq i, j$, $\Gamma_{ijk}^{\alpha\alpha\gamma}$ becomes at least one order of magnitude lower than the

TABLE IV. Diagonal ($\alpha = \beta$, or isotropic) and off-diagonal elements $|\Gamma_{0j0}^{\alpha\beta\gamma}|$ of the SLC matrix of fcc Ni, in units of mRy/Å. Here, j stands for the neighborhood around the reference site. The distance vectors $\vec{r}_{0j}$ are given in units of the lattice parameter, a.

j	$\vec{r}_{0j}$	$|\Gamma_{0j0}^{\alpha\alpha x}|$	$|\Gamma_{0j0}^{\alpha\alpha y}|$	$|\Gamma_{0j0}^{\alpha\alpha z}|$	Off diagonals ($\alpha \neq \beta$)
1	$\frac{1}{2}(0, \pm 1, \pm 1)$	0	0.66	0.66	
	$\frac{1}{2}(\pm 1, 0, \pm 1)$	0.66	0	0.66	
	$\frac{1}{2}(\pm 1, \pm 1, 0)$	0.66	0.66	0	$<0.7\%$
2	$\frac{1}{2}(0, 0, \pm 2)$	0	0	0.013	
	$\frac{1}{2}(0, \pm 2, 0)$	0	0.013	0	
	$\frac{1}{2}(\pm 2, 0, 0)$	0.013	0	0	$\lesssim 20\%$
3	$\frac{1}{2}(\pm 1, \pm 1, \pm 2)$	0.018	0.018	0.031	
	$\frac{1}{2}(\pm 1, \pm 2, \pm 1)$	0.018	0.031	0.018	
	$\frac{1}{2}(\pm 2, \pm 1, \pm 1)$	0.031	0.018	0.018	$\lesssim 3\%$

terms in which $k = i, j$ (for instance, we calculated $|\Gamma_{ijk}^{\alpha\alpha z}| \approx$ 0.03 mRy/Å, considering nearest-neighbor $i \neq j \neq k$ sites). Therefore, we here consider only the $\vec{\Gamma}_{ij(i,j)}$ parameters. For these cases, a first-order polynomial was fitted in the $\mathcal{J}_{ij}(u_i)$ curves in order to extract the SLC parameters. An example of how the isotropic J_{ij} interactions change as a function of atomic displacements for nearest-neighbor Ni-Ni is shown in Fig. 8. In turn, Table IV exhibits the complete list of SLC values up to the third neighboring shell of a given reference site, used as inputs for the heat-conserving three-temperature model. As can be noticed, the off-diagonal terms account for a relatively minor part of the effect; the most important ones are the first neighbor parameters, which vary almost linearly with the atomic displacements (see Fig. 8). However, it is also noteworthy that from the second neighbors the SLC slightly increases, becoming relatively more relevant due to the multiplicity of each shell.

APPENDIX C: DIFFERENCES IN MODEL G COUPLING PARAMETERS

One of the key advantages of the HC3TM over the original 3TM is that the reservoir temperatures are obtained directly

TABLE V. Electron-phonon coupling constants used in literature for fcc Ni.

Reference	G_{el} ($\times 10^{18}$ W m^{-3} K^{-1})
Zahn *et al.* [3]	≈ 1.7–2
Beaurepaire *et al.* [1]	0.8
Koopmans *et al.* [14]	4.05
Dvornik *et al.* [58]	≈ 1.4–3
Wellershoff *et al.* [59]	0.36

from the calculated energies during the dynamics. This eliminates the need for the G_{es}, G_{el}, and G_{sl} coupling parameters used in Eq. (A1), with almost no change in the computational cost. Usually estimated via indirect ways, the evaluation of these parameters results in inconsistent data in the literature. An instructive example can be seen in Table V for G_{el}, for which one finds differences of one order of magnitude. These differences lead to (sometimes significantly) slower or faster reservoir response to the energy flow, affecting the overall demagnetization dynamics.

[1] E. Beaurepaire, J.-C. Merle, A. Daunois, and J.-Y. Bigot, Phys. Rev. Lett. **76**, 4250 (1996).

[2] S. Anisimov, B. Kapeliovich, and T. Perelman, Zh. Eksp. Teor. Fiz **66**, 375 (1974).

[3] D. Zahn, F. Jakobs, Y. W. Windsor, H. Seiler, T. Vasileiadis, T. A. Butcher, Y. Qi, D. Engel, U. Atxitia, J. Vorberger, and R. Ernstorfer, Phys. Rev. Res. **3**, 023032 (2021).

[4] S. Pan, F. Ganss, S. Panda, G. Sellge, C. Banerjee, J. Sinha, O. Hellwig, and A. Barman, J. Mater. Sci. **57**, 6212 (2022).

[5] T. Roth, A. J. Schellekens, S. Alebrand, O. Schmitt, D. Steil, B. Koopmans, M. Cinchetti, and M. Aeschlimann, Phys. Rev. X **2**, 021006 (2012).

[6] V. P. Antropov, M. I. Katsnelson, B. N. Harmon, M. van Schilfgaarde, and D. Kusnezov, Phys. Rev. B **54**, 1019 (1996).

[7] O. Eriksson, A. Bergman, L. Bergqvist, and J. Hellsvik, *Atomistic Spin Dynamics: Foundations and Applications* (Oxford University, New York, 2017).

[8] D. Zahn, F. Jakobs, H. Seiler, T. A. Butcher, D. Engel, J. Vorberger, U. Atxitia, Y. W. Windsor, and R. Ernstorfer, Phys. Rev. Res. **4**, 013104 (2022).

[9] M. Battiato, K. Carva, and P. M. Oppeneer, Phys. Rev. Lett. **105**, 027203 (2010).

[10] F. Willems, C. von Korff Schmising, C. Strüber, D. Schick, D. W. Engel, J. Dewhurst, P. Elliott, S. Sharma, and S. Eisebitt, Nat. Commun. **11**, 871 (2020).

[11] E. Carpene, E. Mancini, C. Dallera, M. Brenna, E. Puppin, and S. De Silvestri, Phys. Rev. B **78**, 174422 (2008).

[12] U. Ritzmann, P. M. Oppeneer, and P. Maldonado, Phys. Rev. B **102**, 214305 (2020).

[13] L. Waldecker, R. Bertoni, R. Ernstorfer, and J. Vorberger, Phys. Rev. X **6**, 021003 (2016).

[14] B. Koopmans, G. Malinowski, F. Dalla Longa, D. Steiauf, M. Fähnle, T. Roth, M. Cinchetti, and M. Aeschlimann, Nat. Mater. **9**, 259 (2010).

[15] R. S. Malik, E. K. Delczeg-Czirjak, R. Knut, D. Thonig, I. Vaskivskyi, R. Phuyal, R. Gupta, S. Jana, R. Stefanuik, Y. O. Kvashnin, S. Husain, A. Kumar, P. Svedlindh, J. Söderström, O. Eriksson, and O. Karis, Phys. Rev. B **104**, L100408 (2021).

[16] J. Hellsvik, D. Thonig, K. Modin, D. Iuşan, A. Bergman, O. Eriksson, L. Bergqvist, and A. Delin, Phys. Rev. B **99**, 104302 (2019).

[17] P.-W. Ma, S. L. Dudarev, A. A. Semenov, and C. H. Woo, Phys. Rev. E **82**, 031111 (2010).

[18] J. Casas-Vázquez and D. Jou, Phys. Rev. E **49**, 1040 (1994).

[19] D. C. Wallace, Am. J. Phys. **40**, 1718 (1972).

[20] M. Dixon, F. Hoare, T. Holden, and D. Moody, Proc. R. Soc. A **285**, 561 (1965).

[21] L. Bergqvist and A. Bergman, Phys. Rev. Mater. **2**, 013802 (2018).

[22] K. Gilmore, Y. U. Idzerda, and M. D. Stiles, Phys. Rev. Lett. **99**, 027204 (2007).

[23] S. M. Bhagat and P. Lubitz, Phys. Rev. B **10**, 179 (1974).

[24] P.-W. Ma, S. L. Dudarev, and C. H. Woo, Phys. Rev. B **85**, 184301 (2012).

[25] R. F. L. Evans, U. Atxitia, and R. W. Chantrell, Phys. Rev. B **91**, 144425 (2015).

[26] P. Tengdin, W. You, C. Chen, X. Shi, D. Zusin, Y. Zhang, C. Gentry, A. Blonsky, M. Keller, P. M. Oppeneer *et al.*, Sci. Adv. **4**, eaap9744 (2018).

[27] B. Frietsch, A. Donges, R. Carley, M. Teichmann, J. Bowlan, K. Döbrich, K. Carva, D. Legut, P. M. Oppeneer, U. Nowak *et al.*, Sci. Adv. **6**, eabb1601 (2020).

[28] S. Mondal and A. Barman, Phys. Rev. Appl. **10**, 054037 (2018).

[29] M. Stiehl, M. Weber, C. Seibel, J. Hoefer, S. T. Weber, D. M. Nenno, H. C. Schneider, B. Rethfeld, B. Stadtmüller, and M. Aeschlimann, Appl. Phys. Lett. **120**, 062410 (2022).

[30] M. Krauß, T. Roth, S. Alebrand, D. Steil, M. Cinchetti, M. Aeschlimann, and H. C. Schneider, Phys. Rev. B **80**, 180407(R) (2009).

[31] P. Maldonado, T. Chase, A. H. Reid, X. Shen, R. K. Li, K. Carva, T. Payer, M. Horn von Hoegen, K. Sokolowski-Tinten, X. J. Wang, P. M. Oppeneer, and H. A. Dürr, Phys. Rev. B **101**, 100302(R) (2020).

[32] S. R. Acharya, V. Turkowski, G. P. Zhang, and T. S. Rahman, Phys. Rev. Lett. **125**, 017202 (2020).

[33] R. Martinho Vieira, O. Eriksson, T. Björkman, A. Bergman, and H. C. Herper, Mater. Res. Lett. **10**, 156 (2022).

[34] P. R. Peduto, S. Frota-Pessoa, and M. S. Methfessel, Phys. Rev. B **44**, 13283 (1991).

[35] S. Frota-Pessoa, Phys. Rev. B **46**, 14570 (1992).

[36] H. P. Wijn, *Magnetic Properties of Metals: d-Elements, Alloys and Compounds* (Springer, New York, 1991).

[37] O. K. Andersen, Phys. Rev. B **12**, 3060 (1975).

[38] H. Petrilli and S. Frota-Pessôa, J. Phys.: Condens. Matter **2**, 135 (1990).

[39] S. Frota-Pessôa, R. B. Muniz, and J. Kudrnovský, Phys. Rev. B **62**, 5293 (2000).

[40] U. von Barth and L. Hedin, J. Phys. C **5**, 1629 (1972).

[41] S. Frota-Pessôa, Phys. Rev. B **69**, 104401 (2004).

[42] N. Beer and D. G. Pettifor, *The Electronic Structure of Complex Systems* (Springer, Boston, 1984), pp. 769–777.

[43] A. I. Liechtenstein, M. Katsnelson, V. Antropov, and V. Gubanov, J. Magn. Magn. Mater. **67**, 65 (1987).

[44] S. Mankovsky, S. Polesya, H. Lange, M. Weißenhofer, U. Nowak, and H. Ebert, Phys. Rev. Lett. **129**, 067202 (2022).

[45] P. Giannozzi, O. Andreussi, T. Brumme, O. Bunau, M. B. Nardelli, M. Calandra, R. Car, C. Cavazzoni, D. Ceresoli, M. Cococcioni *et al.*, J. Phys.: Condens. Matter **29**, 465901 (2017).

[46] A. Togo and I. Tanaka, Scr. Mater. **108**, 1 (2015).

[47] D. Vanderbilt, Phys. Rev. B **41**, 7892 (1990).

[48] H. J. Monkhorst and J. D. Pack, Phys. Rev. B **13**, 5188 (1976).

[49] N. Marzari, D. Vanderbilt, A. De Vita, and M. C. Payne, Phys. Rev. Lett. **82**, 3296 (1999).

[50] O. Eriksson, B. Johansson, R. C. Albers, A. M. Boring, and M. S. S. Brooks, Phys. Rev. B **42**, 2707 (1990).

[51] R. J. Birgeneau, J. Cordes, G. Dolling, and A. D. B. Woods, Phys. Rev. **136**, A1359 (1964).

[52] J. W. Flocken and J. R. Hardy, Phys. Rev. **177**, 1054 (1969).

[53] C. Illg, B. Meyer, and M. Fähnle, Phys. Rev. B **86**, 174309 (2012).

[54] M. Kresch, O. Delaire, R. Stevens, J. Y. Y. Lin, and B. Fultz, Phys. Rev. B **75**, 104301 (2007).

[55] T. Yokoyama and K. Eguchi, Phys. Rev. Lett. **107**, 065901 (2011).

[56] P. C. Liu, P. R. Okamoto, N. J. Zaluzec, and M. Meshii, Phys. Rev. B **60**, 800 (1999).

[57] M. Simerska, Czech. J. Phys. **12**, 858 (1962).

[58] M. Dvornik, A. Vansteenkiste, and B. Van Waeyenberge, Appl. Phys. Lett. **105**, 162411 (2014).

[59] S. S. Wellershoff, J. Gudde, J. Hohlfeld, J. G. Muller, and E. Matthias, *High-Power Laser Ablation* (SPIE, Bellingham, WA, 1998), Vol. 3343, pp. 378–387.